JOURNAL OF SPACECRAFT AND ROCKETS
Vol. 30, No. 5, September–October 1993

HL-20 Computational Fluid Dynamics Analysis

K. James Weilmuenster* and Francis A. Greene†
NASA Langley Research Center, Hampton, Virginia 23681

The essential elements of a computational fluid dynamics analysis of the HL-20/personnel launch system aerothermal environment at hypersonic speeds including surface definition, grid generation, solution techniques, and visual representation of results are presented. Examples of solution technique validation through comparison with data from ground-based facilities are presented, along with results from computations at flight conditions. Computations at flight points indicate that real-gas effects have little or no effect on vehicle aerodynamics and, at these conditions, results from approximate techniques for determining surface heating are comparable with those obtained from Navier-Stokes solutions.

Nomenclature

C_A = axial-force coefficient, axial force/$q_\infty S_{ref}$
C_D = drag coefficient, drag/$q_\infty S_{ref}$
C_m = pitching-moment coefficient, pitching moment/$q_\infty S_{ref} L_{ref}$
C_N = normal-force coefficient, normal force/$q_\infty S_{ref}$
h = altitude, ft
L/D = lift-to-drag ratio
L_{ref} = reference length, ft
M = freestream Mach number
q_w = heat flux, Btu/ft^2-s
q_∞ = freestream dynamic pressure, lbf/ft^2
R = freestream unit Reynolds number, $\rho_\infty V_\infty/\mu_\infty$, /ft
R_L = Reynolds number based on L_{ref}
S_{ref} = reference area, ft^2
T_∞ = freestream temperature, K
T_w = wall temperature, K
V_∞ = freestream velocity, ft/s
z = axial length measured from the nose, ft
α = angle of attack
γ = ratio of specific heats
μ_∞ = freestream viscosity, lbm/ft-s
ρ_∞ = freestream density, lbm/ft^3

Introduction

NASA Langley Research Center has been deeply involved in the definition of a new, cost-effective transportation system that would complement the current Shuttle system and provide manned access to space for the next generation of space programs. The Langley configuration, designated the HL-20, is a lifting body born from work within this vehicle class performed by NASA and the Department of Defense (DOD) in the late 1960s and early 1970s. Sized to satisfy constraints imposed by its initial mission as an emergency evacuation vehicle from Space Station Freedom, the HL-20 is one-quarter the size of the Shuttle and lighter by an order of magnitude. Designed to carry a crew of two and eight passengers for a 72-h mission, the HL-20 is currently a candidate vehicle for the personnel launch system (PLS), with the role of crew exchange at Freedom or placing small payloads into orbit.

Since the inception of the HL-20, computational fluid dynamics (CFD) have played a role in its development. CFD's most important contribution to this effort is in defining the aerothermal environment of the vehicle for conditions where ground-based facilities cannot simulate the flow environment. These conditions are typically encountered during the hypersonic portion of the re-entry trajectory, where chemistry effects within the shock layer influence the heating and pressure on the vehicle's surface.

Before the aerodynamic and thermal characteristics of the vehicle in this flight regime can be numerically investigated, it is important to demonstrate that the software being used is capable of reproducing the results from ground-based facilities. In addition, the need to support this program has driven the development of new and improved software, particularly in the areas of configura-

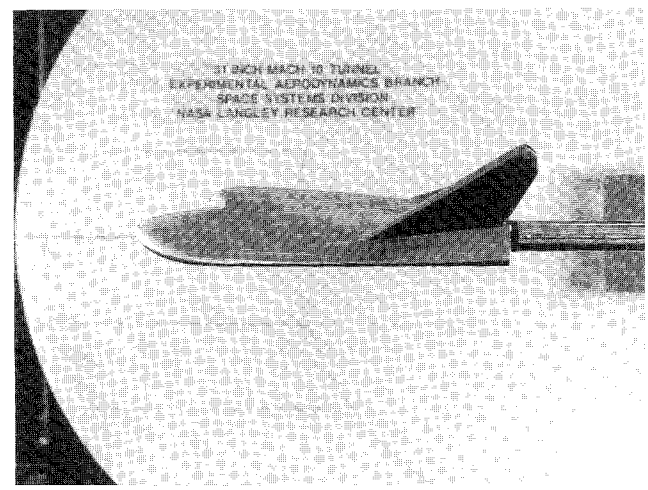

Fig. 1 Model of HL-20 vehicle.

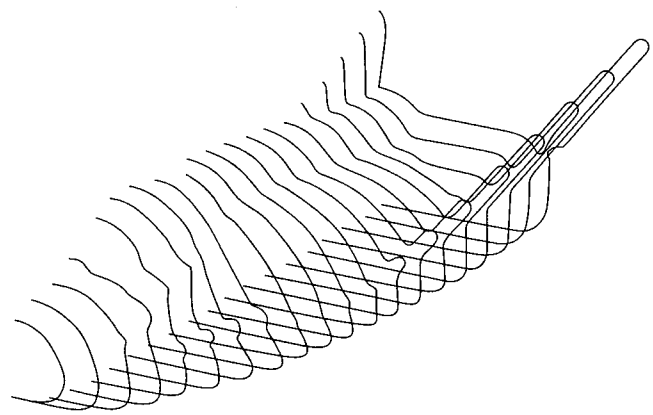

Fig. 2 Original measured surface database.

Received Dec. 1, 1992; revision received Jan. 19, 1993; accepted for publication Jan. 28, 1993.

*Aero-Space Technologist, Aerothermodynamics Branch, Space Systems Division. Associate Fellow AIAA.

†Aero-Space Technologist, Aerothermodynamics Branch, Space Systems Division. Senior Member AIAA.

tion surface definition and grid generation. In the body of this paper, the technology used in the CFD program will be reviewed; CFD results will be compared with measurements taken in ground-based facilities; and CFD predictions of the aerothermal environment at a flight condition will be shown.

Geometry and Grid Generation

Surface Definition

When the HL-20 CFD effort began, a computer-aided design (CAD) representation of the vehicle geometry was not available. Thus, an initial database of cross-sectional coordinates for the configuration was obtained from physical measurements of a wind-tunnel model (Fig. 1). From these measurements, an initial database of 20 cross sections was constructed and is shown in Fig. 2. These cross sections were then used as input to the SMART[1] system, which was used to enrich and smooth the initial database. As shown in Fig. 2, in the database of measured cross sections, the nose of the configuration is ill-defined. The SMART system was used to to create a nose cap that was consistent with the measured surface database. The result was a surface grid of sufficient density but insufficient quality for CFD work. Software was developed to create a surface definition of the quality required for CFD analysis.

The procedures used to create the new surface definition are given in Ref. 2 and briefly outlined here. To remove imperfections in the measured data, a cubic-spline smoothing algorithm was applied to the coordinates in each cross section. Once the cross-sectional data were smoothed, a distribution of points around the body is specified as a function of axial length. Then the desired surface grid is interpolated from the enhanced database and smoothed again based on a prescribed distribution of cross sections. The resulting surface grid, consisting of 81 points in each plane around the vehicle and 125 planes in the axial direction, is shown in Fig. 3.

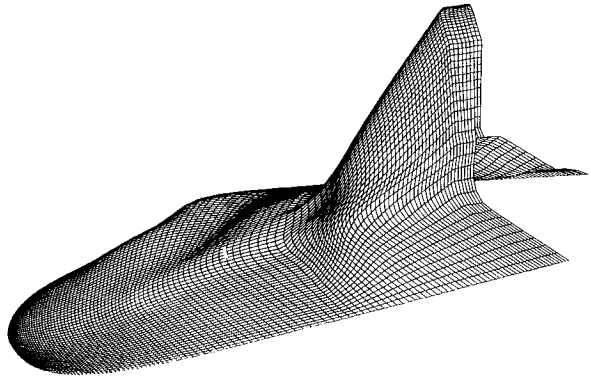

Fig. 3 HL-20 surface grid.

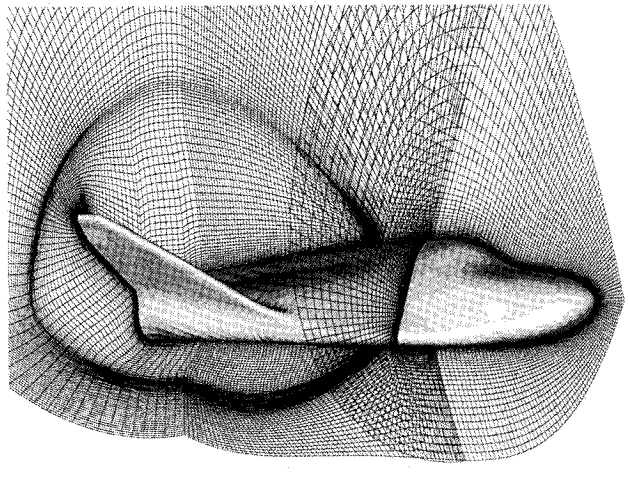

Fig. 4 Composite of grids in symmetry plane and two spanwise surfaces.

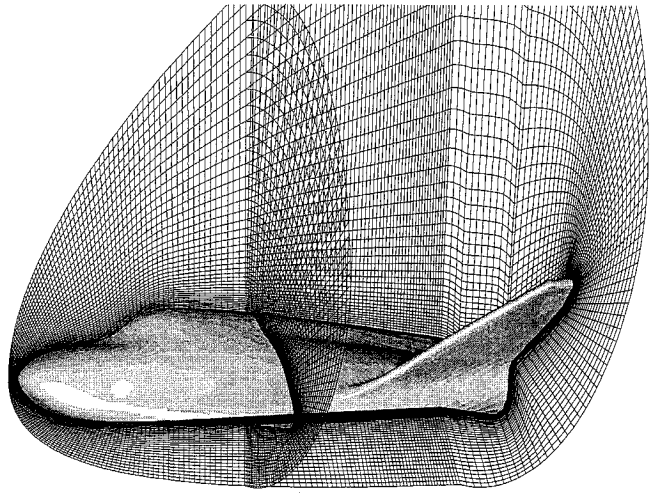

Fig. 5 Volume grid about the HL-20 configuration (single block).

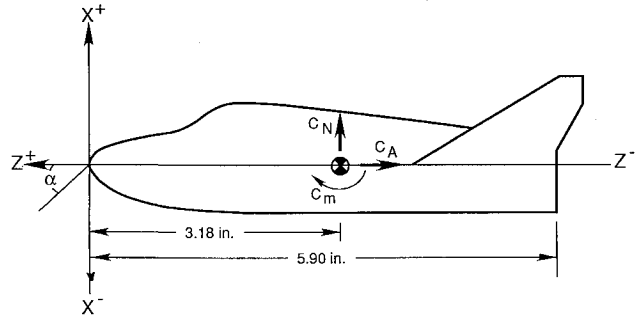

Fig. 6 Coordinate system and aerodynamic coefficient convention.

Volume Grid

The technology for creating volume grids for CFD computations has changed rapidly since HL-20 CFD analysis began. The original volume grid, Fig. 4, is a dual-block topology that is described in detail in Ref. 2. In this grid, there is an inner block that begins at a singularity line just upstream of the wing root and ends at the outflow boundary, thus surrounding the aft portion of the vehicle. The second block surrounds the front part of the vehicle, as well as the inner block. Although this form of volume grid topology significantly reduces the number of points required for the volume grid, the singular line on the body led to some computational difficulties.[3] Thus, the procedure described in Ref. 3 was devised to create the single-block volume grid shown in Fig. 5.

The grids just described have been used extensively for inviscid flowfield solutions. Viscous flow solutions place requirements on the surface and volume grids that cannot be met by the software used to create the inviscid grids. To create the viscous grids, the GRIDGEN[4] software package has been used. This interactive code provides the flexibility to specify the proper orthogonal boundary conditions at the wall, to distribute points on the surface as needed, and to implement smoothing of both the surface and volume grids. For the inviscid and viscous solutions shown in this paper, a 125×125 surface grid has been used, and the volume grid is constructed in one block. For inviscid solutions, 41 points were distributed between the vehicle surface and outer boundary of the grid. For viscous solutions, this number was increased to 93.

Experimental Data

An extensive hypersonic aerothermal database[5,6] for the HL-20 has been established using ground-based facilities at the Langley

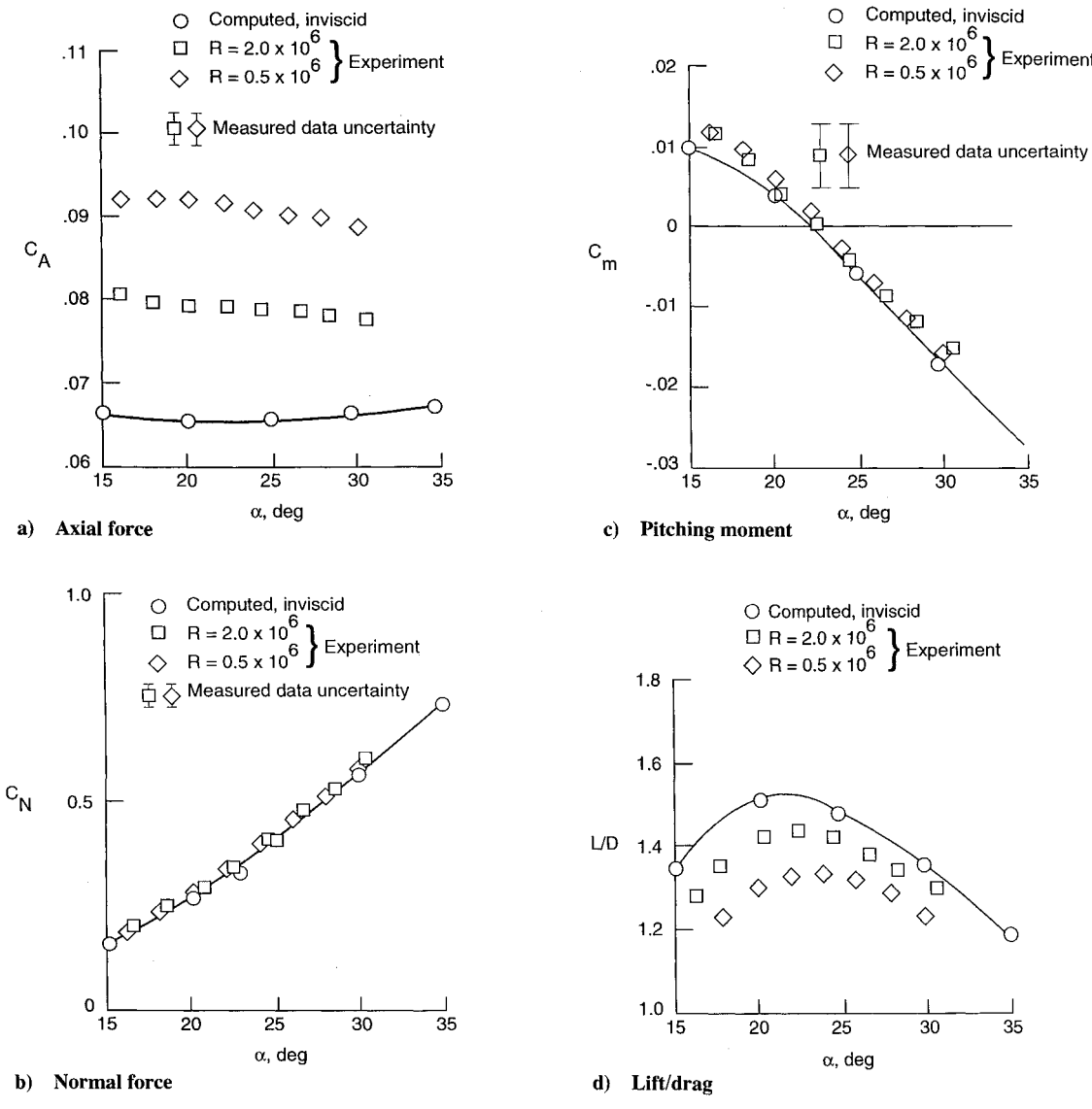

Fig. 7 Comparison of computed, inviscid, and measured aerodynamic coefficients at Mach 10 in air.

Research Center. The experimental data presented in this article were taken in three facilities: the 20-in. Mach 6 tunnel,[7] the 31-in. Mach 10 tunnel,[8] and the hypersonic CF_4 tunnel.[9] All operate in a blowdown mode, with the first two using air and the third tetrafluoromethane (CF_4) as the test gas. The relatively low ratio of specific heats γ associated with CF_4 allows this facility to simulate the large density ratios across a normal shock encountered in flight at hypersonic speeds.

Comparisons of results from the hypersonic CF_4 tunnel, whose nominal operating Mach number is 6, and the 20-in. Mach 6 tunnel give an indication of the effects of low freestream values of γ on the aerodynamics of the vehicle. The inclusion of measurements from the 31-in. Mach 10 tunnel allows Mach number effects to be studied. Force and moment data were taken in all three facilities. Surface thermal mapping and streamline patterns studies were carried out in the air-based facilities.

Numerical Methods

A CFD flowfield analysis yields a great deal of information. Visualization of the external flowfield can highlight important features such as shock impingements and the inception and extent of separated flow. However, most attention is directed to the state of the flow at the vehicle surface. Surface pressures define structural requirements and are integrated along with the viscous forces to produce the aerodynamic characteristics of the vehicle. Surface heating dictates the design of the vehicle's thermal protection system and can lead to modifications to the overall configuration if areas of excessively high heating are encountered. There are several CFD approaches, which are next discussed, for generating the previously given information.

Euler

The main attraction of Euler (inviscid) solutions is that significantly fewer computer resources are required than in a viscous computation and, therefore, they are applicable to parametric studies. Euler methods have been used successfully at hypersonic speeds for the determination of aerodynamics for blunt bodies[10,11] and winged entry vehicles.[12] The Euler solutions give reasonable results for blunt-body aerodynamic coefficients because they are dominated by the surface pressure. For a winged entry vehicle at a high angle of attack, the windward surface acts very much like a blunt body, whereas the leeside flowfield can be very complex, especially if the geometry is complicated. However, pressures on the leeside are orders of magnitude smaller than those on the windside and thus contribute little to the aerodynamic coefficients.

Axisymmetric Analog

The primary product of an Euler solution is surface pressure. However, when an inviscid solution is coupled with the axisymmetric analog technique, surface heating distributions can be determined. In this article, the AA3DBL[13] (axisymmetric analog three-

dimensional boundary-layer) code has been used to generate heating distributions for the HL-20. This code has previously been used for heating calculations on a blunt body[14] and winged entry vehicle.[15]

Surface heating is usually restricted to the windside of the vehicle because of limited applicability of the axisymmetric analog to the leeside flow. This leaves a Navier-Stokes solution as the only means of accessing leeside heating. This does not represent a serious setback since, in general, the highest levels of heating occur on the windward side of the vehicle.

Navier-Stokes

In the mid-1980s, Gnoffo[16] developed a robust TVD scheme for computing the viscous hypersonic flow about blunt bodies. Based on this work, Greene[17] developed an inviscid flow solver for winged entry vehicles that was used for the inviscid solutions presented in this paper. In the same time frame, other codes based on Ref. 16 were being developed to address specific issues associated with hypersonic entry. Recently, all this work has been consolidated and incorporated in the Langley Aerothermodynamic Upwind Relaxation Algorithm (LAURA). This code was used for the viscous computations in this paper.

The LAURA code is a point-implicit, finite-volume solver based on the upwind-biased flux-difference splitting of Roe. The scheme utilizes Yee's symmetric total variation diminishing discretization to achieve second-order spatial accuracy and incorporates Harten's entropy fix. LAURA is capable of modeling Euler and Navier-Stokes flow for a host of different air chemistry assumptions: perfect gas, equilibrium, chemical nonequilibrium, and thermochemical nonequilibrium. In addition, any gas or gas mixture can be addressed as long as there is an adequate model for the thermodynamic and transport properties of the gas in question.

The LAURA code supports a number of boundary conditions. In addition to the usual no-slip conditions at the wall, the code supports the specification of noncatalytic, fully catalytic, and finite-rate catalytic boundary conditions. Also, the wall temperature may be specified as a constant value, fixed distribution, or values based on a radiation equilibrium wall condition.

Navier-Stokes solutions present the best CFD approximation of the flowfield. They do require up to an order-of-magnitude increase in the CPU time and a factor of 2 to 4 increase in CPU memory over that needed for an Euler solution. Weilmuenster[18] has demonstrated a technique for managing these resource-intensive computations. Kleb[19] used these techniques to compute a Shuttle Orbiter solution at a flight condition and make comparisons with in-flight measurements of surface heating on both the wind and leesides of the vehicle. These same procedures have been applied to viscous HL-20 computations.

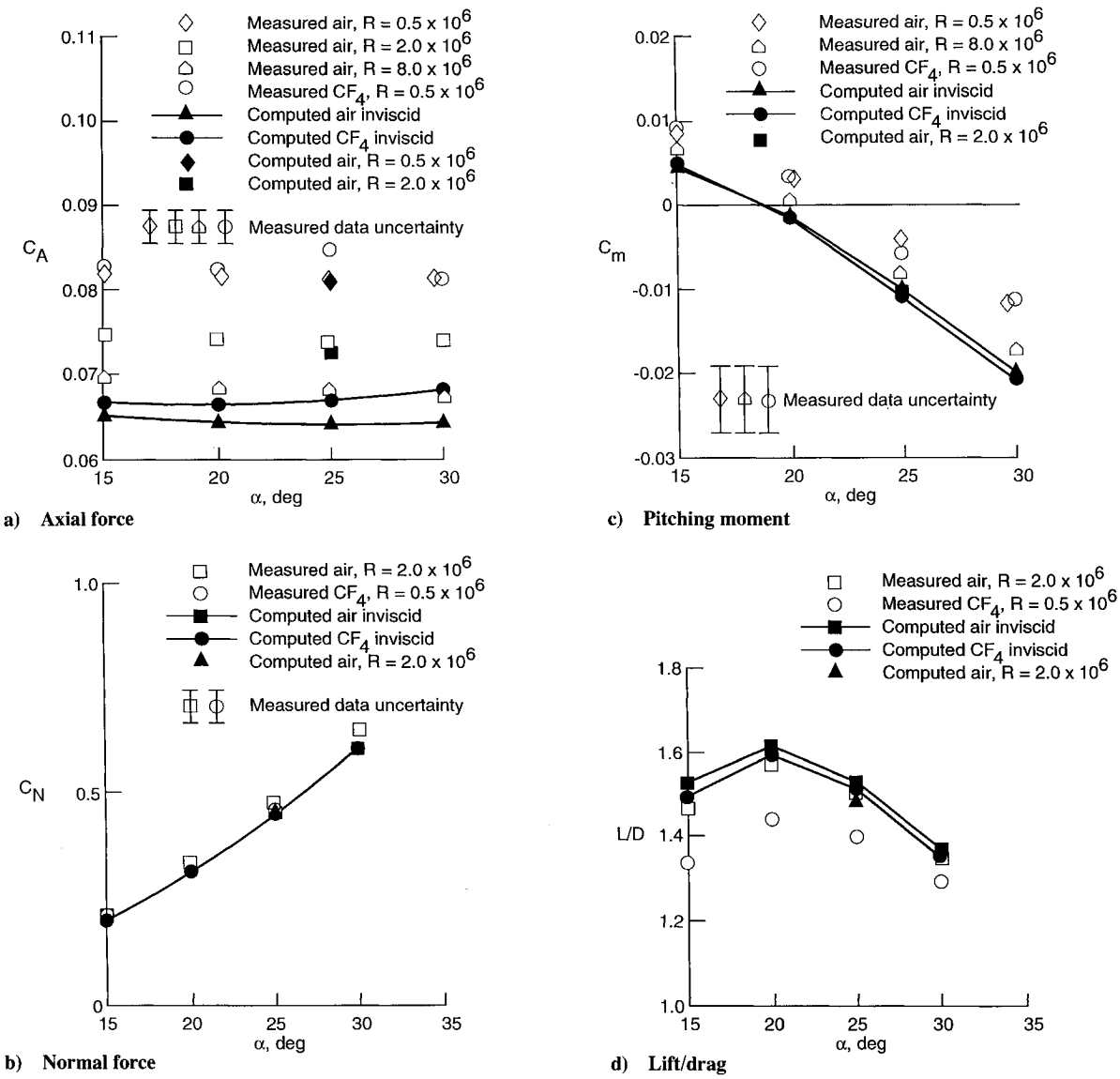

Fig. 8 Comparison of computed and measured aerodynamic coefficients at Mach 6 in air and CF_4.

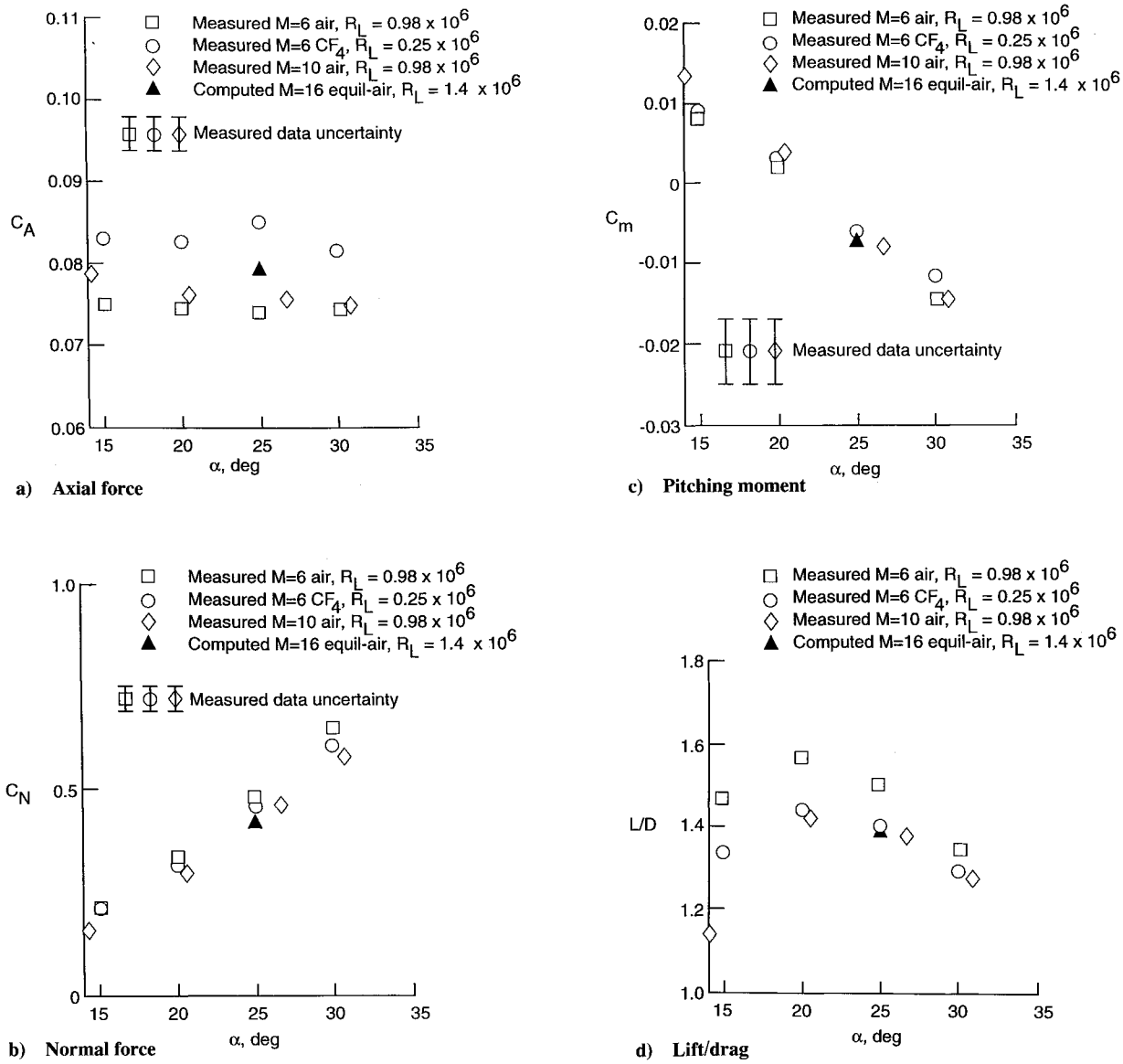

Fig. 9 Comparison of computed aerodynamics at Mach 15.8 based on viscous, equilibrium air chemistry with measured values at Mach 10 in air and Mach 6 in air and CF_4.

Analysis

Aerodynamics

The remainder of this paper will be devoted to examples of the application of various CFD approaches to the analysis of HL-20 aerothermodynamic characteristics. Only selected data from Ref. 5 are utilized in the following examples. Reference should be made to Ref. 5 for a complete compilation of the hypersonic experimental aerodynamic database. The orientation of the tunnel model in the right-hand coordinate system used for these computations, along with the convention for positive aerodynamic coefficients, is shown in Fig. 6. The reference length for the tunnel model is 5.9 in. For flight computations, the model dimensions are scaled based on a full-size model reference length of 25 ft.

The initial CFD effort was directed toward the comparison of aerodynamic coefficients measured in the 31-in. Mach 10 tunnel and those generated from computational results. Previous analyses[10,12] have shown that a perfect-gas analysis is appropriate when comparing computation with data from this tunnel. This initial work then focused on perfect-gas Euler solutions based on a γ, the ratio of specific heats, of 1.4. Data from the tunnel were taken over a range of unit Reynolds number from 0.5×10^6 to 2.0×10^6 for angles of attack 15 deg $\leq\alpha\leq$30 deg. The CFD solutions were run at angles of attack between 15 and 35 deg in 5 deg increments.

For each measured quantity, the uncertainty in that measurement is represented by an error bar placed in each figure. The comparison for axial-force coefficient C_A is shown in Fig. 7a and exhibits a strong Reynolds number effect. The computed values of C_A are low since there is no contribution from the skin friction, but show the right trend as the tunnel data indicate a decreasing C_A with increasing Reynolds number. Comparisons for the normal-force coefficient C_N are shown in Fig. 7b. Unlike C_A, the measured data show no Reynolds number effect and are in excellent agreement with the computed results. Comparisons of the pitching-moment coefficient C_m are shown in Fig. 7c, where again there is no indication of a Reynolds number effect in the tunnel data. Although the computed results lie slightly below the measured data, the two sets of data are in good agreement, except at the lowest angle of attack. These results again demonstrate that, for this class of vehicle at high angles of attack, viscous forces have little impact on the pitching moment and that good estimates of this aerodynamic parameter can be determined from Euler solutions. This, however, is not the case for the lift-to-drag ratio *L/D* as shown in Fig. 7d. Again, the measured data show a Reynolds number effect. As with C_A, the relative trend between the measured and computed values is correct. This plot illustrates that for this vehicle, the *L/D* performance remains relatively constant over a wide range of angle of attack.

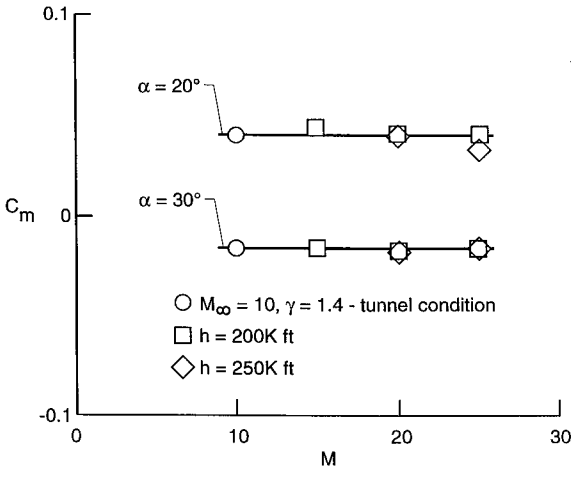

Fig. 10 Pitching moment based on inviscid equilibrium air computations as a function of Mach number and altitude.

During its initial flight, the Shuttle Orbiter experienced a large and unexpected nose-up pitching moment at hypersonic speeds. This deviation from the predicted aerodynamic performance of the vehicle persisted from the onset of continuum flow at Mach 25, down to an altitude of approximately 160,000 ft and Mach 14. This so-called "pitching-moment anomaly" has generally been attributed to real-gas effects,[20] but also there is speculation that the phenomenon is related to body-flap effectiveness. Preliminary engineering analysis indicated that the HL-20 would trim naturally at approximately 28 deg over the hypersonic portion of the entry trajectory. When flying at this attitude, it is important to determine if real-gas effects alter the aerodynamic characteristics of the vehicle as defined by tests in perfect-gas ground-based facilities; if they do, will a ground-based facility such as the hypersonic CF_4 tunnel predict those changes? As a first step to resolving this question, force and moment tests were conducted in the 20-in. Mach 6 tunnel and the hypersonic CF_4 tunnel. At the same time, aerodynamic coefficients were extracted from Euler solutions computed at tunnel conditions. In addition, viscous solutions were run at one angle of attack for two different tunnel conditions.

The comparison of these measured and computed aerodynamics is shown in Fig. 8. The plots of C_A for Mach 6 air, Fig. 8a, show

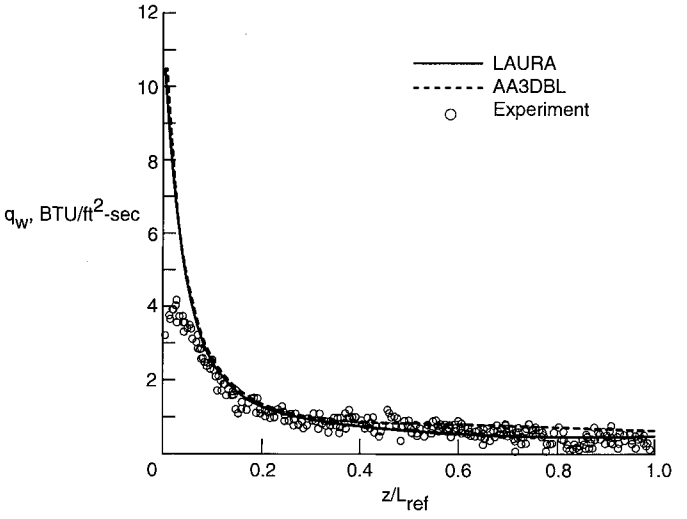

Fig. 11 Comparison of computed and measured centerline surface heating at Mach 5.9, $\alpha = 25$ deg, $T_w = 3000$ K, and $R = 2.3 \times 10^6$.

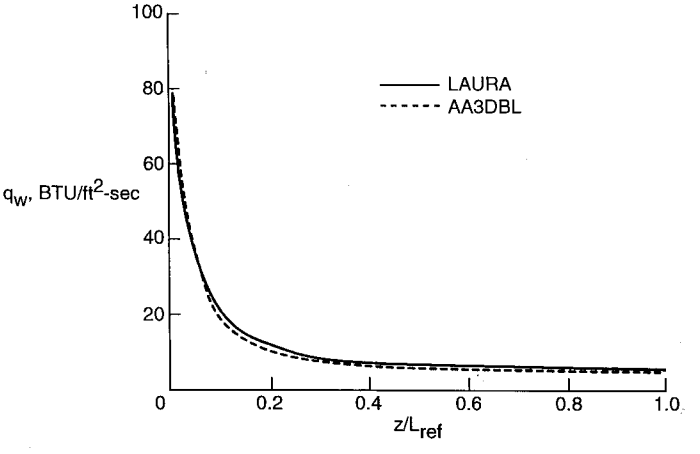

Fig. 12 Navier-Stokes and axisymmetric analog centerline heating at Mach 15.8, $\alpha = 25$ deg, $T_w = 1100$ K, and $R_L = 1.4 \times 10^6$.

the same strong influence of Reynolds number as found at Mach 10. Values of C_A extracted from the Euler solutions for air and CF_4 are only slightly different and lower than the measured data. Measured data at $R = 0.5\times10^6$, 2.0×10^6, and 8.0×10^6 in air and 0.5×10^6 in CF_4 have also been plotted. At $R = 0.5\times10^6$, the air and CF_4 data are almost identical, whereas the higher Reynolds number data tend toward the inviscid limit represented by the Euler (inviscid) solutions. Also, the values of C_A determined from viscous air solutions are shown in this figure. These computed values are in excellent agreement with the tunnel data. A similar plot for C_N, Fig. 8b, shows excellent agreement between the measured and computed values, both viscous and inviscid. The computed results are consistent with the experimental database,[5] which indicated that there was no Reynolds number effect on C_N for either Mach 6 and 10 in air or Mach 6 in CF_4. The Mach 6 air and CF_4 measured and computed values are less consistent than the good agreement found between computed and measured values of C_m at Mach 10. In Ref. 7, the experimental data show no Reynolds number effect on the Mach 10 air or Mach 6 air data. As shown in Fig. 8c, the computed inviscid air and CF_4 results are almost identical, and the viscous solutions show no evidence of Reynolds number effect. On the other hand, the Mach 6 air data are highly dependent on Reynolds number, whereas the CF_4 data agree with the $R = 0.5\times10^6$ air data. Two aspects of the experimental/computational database are difficult to explain: 1) why one out of the three experimental data sets exhibit Reynolds number effects and 2) why aerodynamic coefficients derived from viscous (C_A and C_N) and inviscid (C_N) solutions are in excellent agreement with experimental data while C_m is not. The answer may lie in the accuracy of the pitching-moment measurements. As stated in Ref. 7, the estimated uncertainties in the measured aerodynamic coefficients are given as follows: $C_N = \pm0.03$, $C_A = \pm0.002$, and $C_m = \pm0.004$.

Based on the magnitude of the forces being measured, the uncertainty in C_A and C_N is small, whereas the potential uncertainty in C_m is quite large. These stated uncertainties are based on the minimum dynamic pressure, which is directly proportional to the freestream Reynolds number, in each tunnel. Thus, the greatest uncertainty in the measured values of C_m occurs at the lowest freestream Reynolds numbers. Also, two different balances had to be used in the Mach 6 air tunnel because of the wide range of freestream dynamic pressure covered by the tests. Based on tunnel dynamic pressure and the sensitivity of the balance beams being used, the most accurate measurements of C_m should be at $R = 2.0\times10^6$ and 8.0×10^6 in Mach 6 and 2.0×10^6 in Mach 10 air. Unfortunately, the CF_4 data were taken at conditions likely to produce the least accurate data. With the foregoing facts in mind, the measured and computed values of C_m will all fall within the error band of the experimental data as shown in Figs. 7c and 8c. This would support the assumption that, if there is a Reynolds number effect on pitching moment, it is smaller than the accuracy to which data can be measured and that the most accurate data are in very good agreement with the computed results, which show no Reynolds number effect. The comparison of measured and computed values of L/D is shown in Fig. 8d. Here, as with Mach 10, the computed inviscid results are too high. The L/D for the computed viscous solution is in good agreement with the experimental data.

Fig. 13 Windward surface distribution of log (q_w) at Mach 15.8, α = 25 deg, T_w = 1100 K, and $R_L = 1.4\times10^6$.

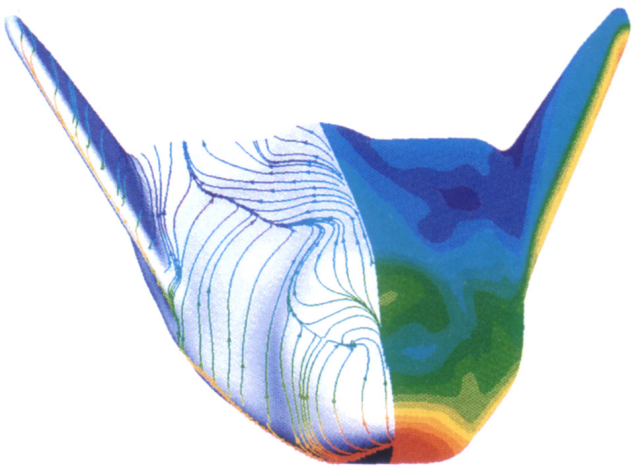

Fig. 14 Leeside composite plot of surface pressure and streamlines at Mach 15.8, α = 25 deg, $R_L = 1.4\times10^6$.

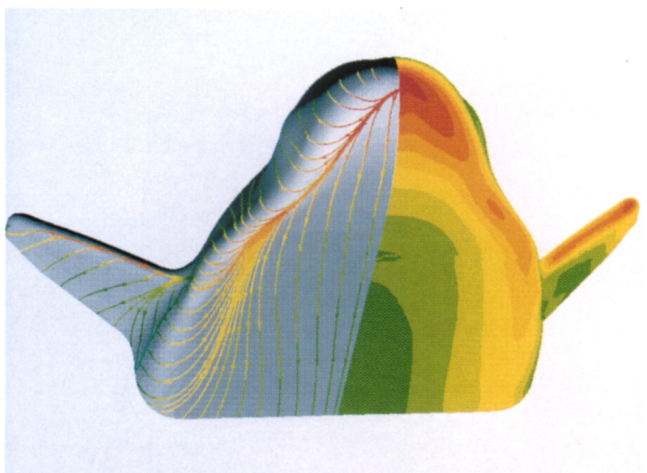

Fig. 15 Windside composite plot of log (q_w) and streamlines at Mach 15.8, α = 25 deg, T_w = 1100 K, and $R_L = 1.4\times10^6$.

The comparison of wind-tunnel and computed aerodynamics just shown illustrates the capability of CFD to model the aerodynamic characteristics of a configuration at wind-tunnel conditions for both a perfect-gas air and CF_4 gas. To determine if the aerodynamic characteristics of the vehicle can be defined by tests in ground-based facilities or will be altered by real-gas effects, a viscous, equilibrium air chemistry solution was run at a flight condition and the extracted aerodynamic coefficients compared with wind-tunnel data. The flight condition of Mach 15.8 and h = 180 k ft was taken from a nominal HL-20 trajectory. The angle of attack of 25 deg was chosen to match a wind-tunnel data point. At this flight point, the full-scale Reynolds number based on body length is approximately 1.3×10^6. Based on model length, equivalent Reynolds number data are available at Mach 6 and 10 in air, whereas the largest Reynolds number available in CF_4 is 0.25×10^6. The measured data are compared with the computed result in Fig. 9, where once again, the uncertainty in the measured data is represented by the error bar in each figure. For each of the aerodynamic coefficients, there is no significant difference between the experimental data and computed values at flight point.

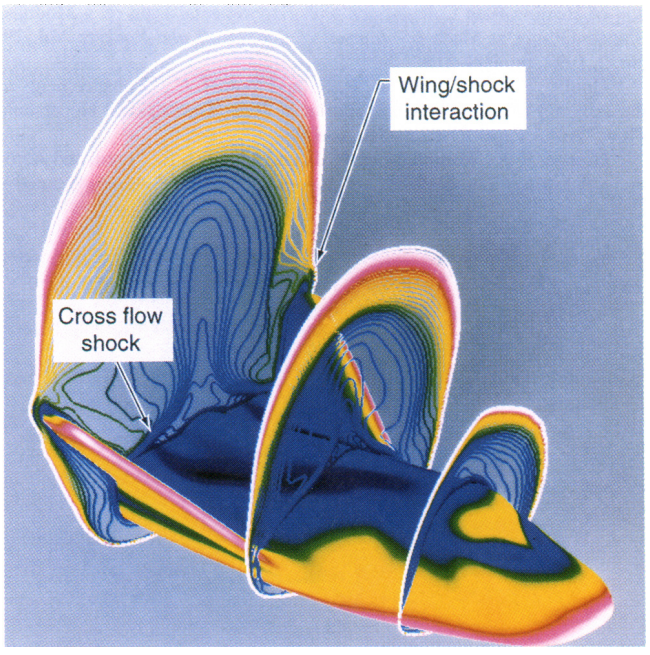

Fig. 16 Surface plot of log (q_w) and planar Mach number contour plots at Mach 15.8, α = 25 deg, T_w = 1100 K, and $R_L = 1.4\times10^6$.

Based on the comparisons, it appears that real-gas effects will not affect the aerodynamics of the HL-20. This viscous computation at the flight condition is made near the lower bound for altitude and Mach number above which real-gas effects become important. A number of additional inviscid computations have been made at higher altitudes and Mach numbers to further check for real-gas effects. Computations were made at several Mach numbers for angles of attack of 20 and 30 deg and altitudes 200 k and 250 k ft, respectively. The resultant values of C_m are plotted in Fig. 10 where, for reference, the computed inviscid value of C_m at Mach 10 is plotted for each angle of attack. Over the spectrum of conditions run, the values of C_m deviate little from the Mach 10, perfect-gas data and exhibit none of the nose up pitching-moment characteristics of the Shuttle Orbiter.

Surface Heating

As can be the case for aerodynamics, the heating environment for an entry vehicle traveling hypersonically can be significantly different than that predicted by tests in ground-based facilities. The procedure here is to first validate the computational procedures with wind-tunnel data and then perform computations at a flight point to determine the surface heating at that condition. Two computational procedures have been used to define surface heating. The first couples the axisymmetric analog with an inviscid solution, whereas the second is a thin-layer Navier-Stokes computation. The flight point corresponds to the same condition used in the aerodynamic calculations, and the solutions are based on the equilibrium air chemistry condition.

Figure 11 shows the comparison of computed and measured centerline surface heating at Mach 6 and 25-deg angle of attack. Results from both the computational techniques are in good agreement with the Mach 6 experimental data (obtained using the thermographic phosphor[6] technique), except in the immediate stagnation region where the working range of the phosphor was exceeded. Computed centerline heating at the flight point is shown in Fig. 12. Both the axisymmetric analog and Navier-Stokes calculations produce the same heating at this condition. Note that at flight, the heating is a factor of 8 higher than the wind-tunnel condition. The distribution of heating on the windside of the vehicle for the flight Navier-Stokes solution is shown in Fig. 13, where a color contour plot of the log of the surface heating is displayed with white representing the highest and blue the lowest values of heating. As expected, the nose, body chine, and wind leading edge experience the highest heating.

Visualization

Although line plots are the standard method for presenting data, a three-dimensional representation of both surface and external flowfield properties is a powerful tool for analyzing flowfield solutions. The following plots of the flight condition Navier-Stokes solution have been prepared using the TECPLOT and FAST software run on Silicon Graphics and Sun Microsystems platforms. In Fig. 14, a view of the leeside of the vehicle is shown. On the left side, the surface streamlines are superimposed on the shaded surface of the vehicle. The changing colors along each streamline represent the local pressure, whereas the arrows indicate the direction of flow. This view reveals the complexity of the leeside flow. In particular, it is easy to follow the lines of flow separation and reattachment. On the right-hand side of the vehicle, a surface pressure contour plot has been constructed. A similar plot for the windside of the vehicle is shown in Fig. 15. Here, the log of the surface heating replaces the surface pressure as the contoured variable. The character of the external flowfield can also be visualized as shown in Fig. 16. In this figure, the contours of the log of surface heating are imposed on the vehicle surface, while Mach number contour plots are shown in each of three planes along the body. In the first plane, the leeside crossflow shock near the centerline is just beginning to form and is better defined in the second plane. In the third plane, the crossflow shock is very distinct. Also, another shock has formed just inboard of the wing. Finally, the topology of the outer shock envelope shows that the bow shock has interacted with the wing to form a bow-shock/wing-shock interaction.

Concluding Remarks

This article has outlined the steps taken in the CFD analysis of the HL-20/PLS aerothermal environment at hypersonic speeds. In this process, care has been taken to validate techniques and procedures through the comparison of computed results with measurements in ground-based facilities. When these validated techniques are applied at flight conditions, they indicate that real-gas effects have little or no effect on vehicle aerodynamics and that the surface heating derived from the Navier-Stokes solution and the approximate technique are consistent. In addition, examples have been shown to demonstrate the effectiveness of the three-dimensional visualization of the computed flowfields.

References

[1]McMillin, M., Reeder, J., Schwing, J., Mills, G., Krisp, V., and Spangler, J., "A Solid Modeler for Aerospace Vehicle Preliminary Design," AIAA Paper 87-2901, Sept. 1987.

[2]Weilmuenster, K. J., Smith, R. E., and Greene, F. A., "Numerical Analysis and Simulation of a Assured Crew Return Vehicle Flow Field," NASA TP-3101, Sept. 1991.

[3]Weilmuenster, K. J., Smith, R. E., and Everton, E. L., "Gridding Strategies and Associated Results for Winged Entry Vehicles," *Proceedings of the 3rd International Conference on Numerical Grid Generation in Computational Fluid Dynamics and Related Fields,* Barcelona, Spain, June 1991, pp. 217–228.

[4]Steinbrenner, J., Chawner, J., and Pouts, C., "Multiple Block Grid Generation in the Interactive Environment," AIAA Paper 90-1602, June 1990.

[5]Micol, J. R., "Experimental and Predicted Aerodynamic Characteristics of a Proposed Assured Crew Return Vehicle (ACRV) Lifting-Body Configuration at Mach 6 and 10," AIAA Paper 90-1403, June 1990.

[6]Horvath, T. J., Rhode, M. N., and Buck, G. M., "Aerothermodynamic Measurements on a Proposed Assured Crew Return Vehicle (ACRV) Lifting Body Configuration at Mach 6 and 10," AIAA Paper 90-1744, June 1990.

[7]Miller, C. G., III, and Gnoffo, P. A., "Pressure Distributions and Shock Shapes for 12.84/7 On-Axis and Bent Nose Biconics in Air at Mach 6," NASA TM-83222, 1981.

[8]Miller, C. G., III, "Measured Pressure Distributions, Aerodynamic Coefficients, and Shock Shapes on Blunt Bodies at Incidence in Hypersonic Air and CF_4," NASA TM-84489, 1982.

[9]Midden, R. E., and Miller, C. G., III, "Description and Calibration of the Langley Hypersonic CF_4 Tunnel—A Facility of Simulating Low Flow

as Occurs for a Real Gas," NASA TP-2384, March 1985.

[10]Weilmuenster, K. J., and Hamilton, H. H., II, "A Comparison of Computed and Measured Aerodynamic Characteristics of a Proposed Aeroassist Flight Experiment Configuration," AIAA Paper 86-1366, June 1986.

[11]Weilmuenster, K. J., and Gnoffo, P. A., "Aeroassisted Flight Experiment Aerodynamic Characteristics at Flight Conditions," *Journal of Spacecraft and Rockets*, Vol. 27, No. 6, 1990, pp. 684–686.

[12]Micol, J. R., and Weilmuenster, K. J., "Experimental Aerodynamic Coefficients on a Shuttle Like Vehicle at Mach 6 and 10 and Comparison to Prediction," AIAA Paper 85-1796, Aug. 1985.

[13]Hamilton, H. H., II, DeJarnette, F. R., and Weilmuenster, K. J., "Application of Axisymmetric Analog for Calculating Heating in Three-Dimensional Flows," *Journal of Spacecraft and Rockets*, Vol. 24, No. 4, 1987, pp. 296–302.

[14]Hamilton, H. H., II, and Weilmuenster, K. J., "Calculation of Convective Heating on Proposed Aeroassist Flight Experiment Vehicle," AIAA Paper 86-1308, June 1986, pp. 208–215.

[15]Hamilton, H. H., II, Greene, F. A., and Weilmuenster, K. J., "Comparison of Heating Rate Calculations with Experimental Data on a Modified Shuttle Orbiter at Mach 6," *Journal of Spacecraft and Rockets*, Vol. 29, No. 2, 1992, pp. 208–215.

[16]Gnoffo, P. A., McCandless, R. S., and Yee, H. C., "Enhancements to the Program LAURA for Computation of Three-Dimensional Hypersonic Flow," AIAA Paper 87-0280, Jan. 1987.

[17]Greene, F. A., Weilmuenster, K. J., and Micol, J. R., "Predicted Aerodynamics for a Proposed Personnel Launch Vehicle," AIAA Paper 90-1668, June 1990.

[18]Weilmuenster, K. J., and Gnoffo, P. A., "Solution Strategies and Heat Transfer Calculations for Three-Dimensional Configurations at Hypersonic Speeds," AIAA Paper 92-2921, June 1992.

[19]Kleb, W. L., and Weilmuenster, K. J., "Characteristics of the Shuttle Orbiter Leeside Flow During a Reentry Condition," AIAA Paper 92-2951, June 1992.

[20]Griffith, B. J., Maus, J. R., and Best, J. T., "Explanation of the Hypersonic Longitudinal Stability Problem—Lessons Learned," NASA CP-2283, March 1983.